Design of a Flutter Suppression System for an Experimental Drone Aircraft

Jerry R. Newsom*
NASA Langley Research Center, Hampton, Virginia
and
Anthony S. Pototzky†
Kentron International, Inc., Hampton, Virginia
and
Irving Abel‡
NASA Langley Research Center, Hampton, Virginia

This paper describes the design of a flutter suppression system for a remotely-piloted research vehicle. The modeling of the aeroelastic system, the methodology used to synthesize the control law, the analytical results used to evaluate the control law performance, and ground testing of the flutter suppression system onboard the aircraft are discussed. The major emphasis is on the use of optimal control techniques employed during the synthesis of the control law.

Nomenclature

G_a = antisymmetric filter
G_c = common filter
G_s = symmetric filter
J = cost function
K_a = antisymmetric gain
K_s = symmetric gain
M = Mach number
M_{fa} = FSS-off flutter Mach number, antisymmetric
M_{fs} = FSS-off flutter Mach number, symmetric
q = dynamic pressure
s = Laplace variable
w_g = gust velocity
δ = control surface deflection, + down
δ_c = actuator command
ϕ_m = phase margin
ζ_D = denominator damping ratio
ζ_N = numerator damping ratio
ω_D = denominator frequency
ω_N = numerator frequency

Matrices

A = plant dynamics matrix
B_1 = plant control distribution matrix
B_2 = plant disturbance distribution matrix
C = plant output distribution matrix
K = full-state feedback gain matrix
L = Kalman estimator gain matrix
Q = output weighting matrix
R = control weighting matrix
u = actuator command vector
X = state vector
X_A = actuator state vector
X_{AC} = aircraft state vector
X_w = turbulence state vector
$\hat{X}$ = estimate of state vector
Y = output vector
η_c = control process noise vector
η_g = gust disturbance noise vector
η_m = measurement noise vector

Dots over symbols denote derivatives with respect to time.

Presented as Paper 83-0990 at the AIAA/ASME/ASCE/AHS 24th Structures, Structural Dynamics and Materials Conference, Lake Tahoe, Nev., May 2-4, 1983; received Sept. 10, 1983; revision received Jan. 18, 1985. This paper is declared a work of the U.S. Government and therefore is in the public domain.

*Assistant Head, Aeroservoelasticity Branch, Loads and Aeroelasticity Division. Member AIAA.
†Engineering Specialist, Aerospace Technologies Division. Member AIAA.
‡Technical Assistant, Office of Director for Structures.

Introduction

A CONSIDERABLE amount of research has been conducted in the application of active controls to increase aircraft flutter speeds. Active flutter suppression has been shown to offer significant advantages over the traditional passive means of solving flutter problems.[1] To take full advantage of this technology, control law synthesis and analysis must be an integral part of aircraft design. This requires the use of synthesis methodologies and associated design aids that will enable the engineer to efficiently synthesize and analyze active flutter suppression systems (FSS). Recently, optimal control theory and optimization techniques have been demonstrated to be efficient, viable, and systematic methods for synthesizing flutter suppression control laws.[2-6]

The need to experimentally validate these synthesis methods is important for general acceptance. A limited number of experimental validations have been performed.[7-11] A majority of these validations have been performed with wind-tunnel models. As a complement to wind-tunnel studies, flight tests of a number of aeroelastic research wings are being conducted with a remotely-piloted research vehicle in a NASA program called Drones for Aerodynamic and Structural Testing (DAST).[12] One of the objectives of this flight program is to evaluate the performance of active flutter suppression. This program provides an excellent opportunity to validate control law synthesis and analysis methods. References 13-15 describe previous test results of the first research wing (ARW-1). After experiencing severe wing damage from the third test flight, the wing was rebuilt and designated ARW-1R.[16]

The purpose of this paper is to describe the overall process used to design the new flutter suppression system for the ARW-1R vehicle.

Description of Aircraft

The general configuration of the vehicle is shown in Fig. 1. The aeroelastic research wing, which has an aspect ratio

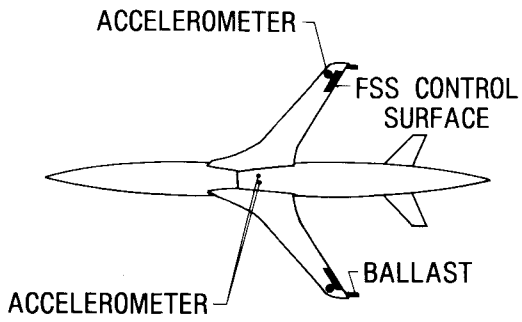

Fig. 1 DAST vehicle.

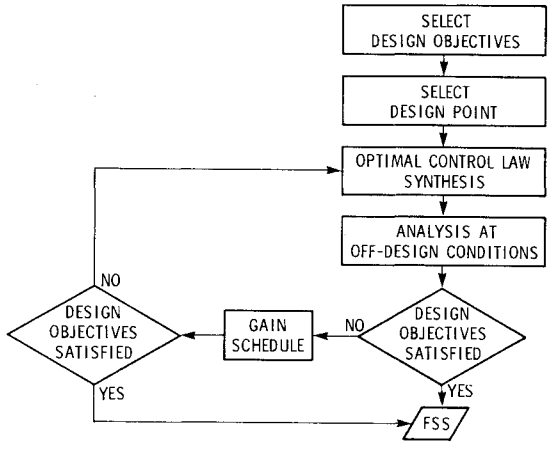

Fig. 2 Flow chart of overall control law design.

of 6.8 and a supercritical airfoil shape, was purposely designed to flutter within the flight envelope. A 2.2. lb. ejectible ballast was placed aft of the rear spar near each wing tip to reduce the flutter speed and to act as a "flutter stopper" upon ejection. The FSS uses four accelerometers and two control surfaces as shown in Fig. 1. The two accelerometers located near the control surfaces measure motions of the wing, and the two in the fuselage near the c.g. are used to measure rigid-body motions. The control surfaces serve the dual functions of suppressing flutter through the FSS and of providing known excitation to the wing.

Structural and Aerodynamic Modeling

During the wing rebuilding process, it was decided that a new finite-element model[17] would be developed using the Engineering Analysis Language (EAL).[18] Where it was considered advantageous, the EAL model borrowed heavily from a previous NASTRAN model. Where there were shortcomings in the earlier model, EAL was used to remodel those areas.

The generalized aerodynamic force coefficients representing the unsteady aerodynamics are computed by using the Doublet Lattice module of the Interaction of Structures, Aerodynamics, and Controls program.[19] The aerodynamic coefficients for the first 10 structural modes, a control surface rotation mode, and a sinusoidal gust are computed for a range of reduced frequencies from 0.0 to 1.2. The reduced frequencies of open- and closed-loop flutter range between 0.1 and 0.16. The areodynamics are calculated from $M=0.700$ to 0.925 at increments of 0.025.

Flutter Suppression System Design

Methodology

A flow chart of the overall control law design process is shown in Fig. 2. The first element of the process is the selection of design objectives (i.e., gain margin, phase margin, etc.). The second element is the selection of a design point

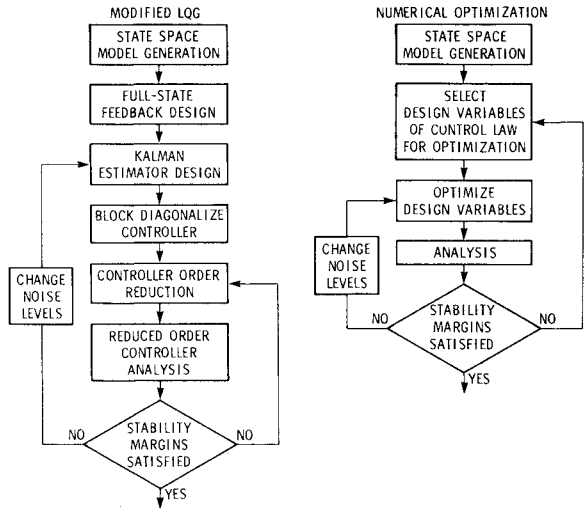

Fig. 3 Flow charts of optimal control laws synthesis approaches.

(i.e., Mach number and altitude). Control law synthesis is then performed at the design point using optimal control methods. Two different approaches to this key element will subsequently be described in some detail. The next element, analysis, provides information on the performance of the control law at off-design flight conditions. If the design objectives at the off-design flight conditions are not met, then a gain scheduler which may be a function of Mach number and/or dynamic pressure is evaluated. If a gain scheduler will not meet the design objectives, then a path back to control law synthesis is selected.

In this paper, two different approaches to the optimal control law synthesis element are described. Flow charts of these two different approaches are given in Fig. 3. The choice of an approach usually depends on what state the overall design process is in.

Both approaches start with the generation of a state space model. This model consists of the airplane dynamic model, actuator model, and the gust disturbance model[5] and can be expressed in equation form as:

$$\dot{X}=AX+B_1u+B_2\eta_g \tag{1}$$

$$Y=CX+\eta_m$$

where

$$X=\begin{Bmatrix} X_{AC} \\ X_A \\ X_w \end{Bmatrix}$$

is the state vector; u is the actuator command vector; η_g is the gust disturbance noise vector; Y is the output vector; and η_m is the measurement noise vector. The state space model is usually of high order. It is not unusual to have 60 or more states. For control law synthesis, it is desirable to have a model with as low an order as possible. Modal residualization[5] is used to construct a lower order "design model" for control law synthesis. The control law synthesized using this model is then analyzed using the higher order "evaluation model."

Modified Linear Quadratic Gaussian (MLQG) Approach

When there is no prior knowledge of a control law definition, the MLQG approach[4,5] shown in Fig. 3 is selected. After

the state space model is generated, the next step in this approach is a full-state feedback design. Full-state feedback provides for the minimization of a quadratic cost function of the output and control vectors. To find the optimal full-state feedback control law, the quadratic cost function (E is the expectation operator) is

$$J = E[\,Y^T Q Y + u^T R u\,] \tag{2}$$

minimized. Initial choice of values for Q and R matrices are model dependent and are regarded as design parameters (see Numerical Results section). This leads to a control law of the form

$$u = -KX \tag{3}$$

where K is the full-state feedback gain matrix. This control law requires that all of the state variables be fed back. Direct measurement of all state variables is not feasible. Therefore, in the next step, a Kalman estimator is used to estimate the state variables from available measurements.

Systems designed using full-state feedback have good gain and phase margins and a desirable low bandwidth. However, systems designed using a Kalman estimator can have poor gain and phase margins and an undesirable high bandwidth. To improve the stability margins during the Kalman estimator design, the input noise adjustment procedure of Doyle and Stein[20] is used. This procedure involves adding a fictitious process noise [η_c in Eq. (4)] directly to the control input of the plant during the estimator design. In addition, varying the measurement noise intensity [η_m in Eq. (4)] during the Kalman estimator design is used to change the bandwidth. The equations of motion are given by

$$\dot{X} = AX + B_1 u + B_1 \eta_c + B_2 \eta_g$$

$$Y = CX + \eta_m \tag{4}$$

Here η_g and η_m are the disturbance, and measurement noise and η_c is the fictitious process noise added at the control input. The estimator dynamics are given by

$$\dot{\hat{X}} = (A - B_1 K - LC)\hat{X} + LY \tag{5}$$

where L is the Kalman estimator gain matrix. Derivation of the gain matrix L can be found in many texts.[21] The design of the estimator involves iterating on the intensities of the fictitious process noise and the measurement noise to obtain a compromise between good stability margins, low bandwidth, and good response characteristics.

The Kalman estimator together with the full-state feedback gain matrix constitute the optimal controller. The Kalman filter and, therefore, the optimal controller will have the same order as that of the model used for the synthesis. In the case of a flexible airplane that contains a large number of structural modes, unsteady aerodynamic lag states, and actuator states, the high order of the optimal controller imposes an unnecessary implementation burden. Several references[3-5] have shown that a reduced-order controller that approximates the full-order optimal controller can be found and with little degradation in the closed-loop performance. The next two steps in this synthesis approach involve reducing the order of the optimal controller.

The transformation of the controller to block diagonal form is used to help select the states that are to be retained during the controller reduction process. A modal residualization technique is then used to reduce the order of the controller. The selection of the states to be retained (and thus the order) during the residualization process is based on engineering judgment.

The reduced-order controller is the analyzed with the "evaluation model" to assess its stability margins. If the margins are unacceptable, then there are two paths that can be taken. The order reduction process can be repeated with a different selection of states to be retained, or the noise intensities can be changed and the Kalman estimator design repeated. The selection of which path to take is again based on engineering judgment.

Numerical Optimization Approach

This approach is used when, for example, changes to the mathematical model occur and it is necessary to update a previously developed control law. The first step in this approach is to generate the state space model. The next step is the selection of design variables (e.g. coefficients of numerator and denominator polynomials) in the control law which are to be optimized.

Next, the design variables are optimized by minimizing a quadratic cost function of the same form as that used during the full-state feedback design. Gradients of the cost function with respect to design variables in the control law are determined by solving a pair of Lyapunov equations. Using the gradients, a nonlinear programming algorithm is used to search for the control law design variables that minimize the cost function. The input noise procedure previously described is used to improve the stability margins of the system.

The optimized control law is then analyzed with the "evaluation model" to examine its performance. If the design objectives are not met then there are two paths that can be taken. A different set of design variables can be selected or the noise intensities can be changed and the optimization and analysis steps repeated. The selection of which path to take is again based on engineering judgment.

Numerical Results

For the following analysis, the first ten symmetric and antisymmetric modes, frequencies, and generalized masses from the EAL structural model are used. Based on the EAL model, the flutter characteristics are established and a control law is designed to provide a 10% increase in flutter speed. The effect of updating the EAL model (due to ground vibration tests) on the performance of the active control system is also discussed.

Basic Characteristics

The predicted symmetric and antisymmetric flutter boundaries (FSS-off) are shown in Fig. 4. The flutter frequencies, which are also shown in Fig. 4, decrease gradually with Mach

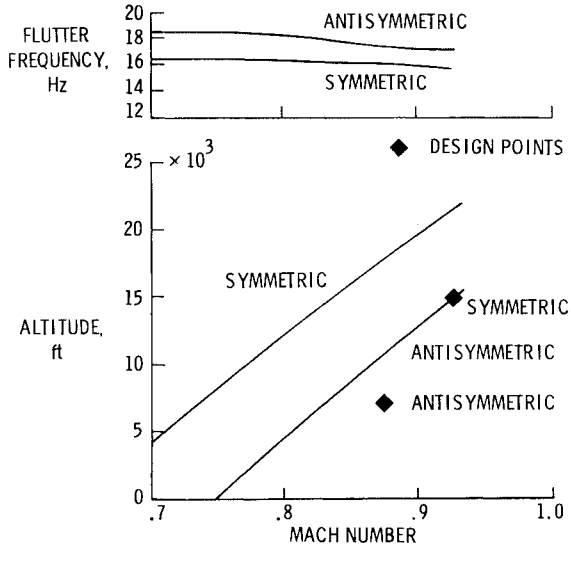

Fig. 4 Predicted FSS-off flutter boundaries and frequencies.

number. (These flutter boundaries should not be compared to those presented in Ref. 14, since both the mathematical model and the wing construction have been changed.) For both the symmetric and antisymmetric cases, the critical mode is first wing bending. The antisymmetric flutter speed is approximately $M=0.09$ greater than the symmetric flutter speed.

MLQG Control Law Synthesis

The first design objective for the FSS is to provide a 10% increase in the minimum flutter speed (the minimum flutter speed is associated with symmetric motion) above that with the FSS-off. Flight tests are to be conducted between the altitudes of 10,000 and 20,000 ft. Therefore, 15,000 ft was arbitrarily selected to be the symmetric design point altitude. At 15,000 ft, the design Mach number was selected as $M=0.925$ ($1.10\times M_{f_S}$). The symmetric design point (as shown in Fig. 4) lies very close to the antisymmetric flutter boundary. If the relative spacing between the symmetric and antisymmetric flutter boundaries is correct, the objective of demonstrating a 10% increase in the minimum flutter speed could be accomplished without the need for implementing an antisymmetric FSS. To protect against possible errors in this spacing, it was decided to define an antisymmetric design point and synthesize an antisymmetric FSS. The antisymmetric design point was defined in the following manner: 1) the symmetric flutter Mach number at 15,000 feet is approximately $M=0.83$; 2) at $M=0.83$, the antisymmetric flutter altitude is approximately 7,000 ft; 3) at 7,000 ft, the antisymmetric FSS is required to provide an increment in flutter Mach number of 0.05. Additional design objectives are that both the symmetric and antisymmetric FSS provide ± 6 *dB* gain margins and ± 30 deg phase margins at speeds up to and including the 10% increase in the minimum flutter speed.

The state space equations are developed in the same manner as described in Ref. 14. The "evaluation model" contains 66 states. There are 20 structural states (10 modes), 40 aerodynamic states (4 lag states per structural mode), 4 actuator states, and 2 gust states. The actuator and Dryden gust models are given in transfer function form as:

$$\frac{\delta}{\delta_c}=\frac{1.69\times 10^{10}}{(s^2+76.78s+87202)(s^2+589.4s+1.93\times 10^5)}$$

$$\frac{w_g}{\eta_g}=\frac{(1.057s+0.239)}{(S^2+0.77s+0.148)} \qquad (6)$$

The "design model" contains 24 states. This model is developed by retaining the states associated with the first three structural modes and residualizing the states associated with the last seven structural modes. The actuator and gust states are retained in the "design model." A direct comparison of the frequency response of the two models matched well over the design range of frequencies for both the symmetric and antisymmetric conditions (not shown).

A full-state feedback control law was designed using a quadratic performance function which weights only the control input. This control law reflects the unstable poles about the imaginary axis and does not affect the other poles. It also has the property that it is the control law that stabilizes the system with the least amount of control input. A Kalman estimator was designed and combined with the full-state feedback gain matrix to generate a 24th order optimal controller. The controller was then reduced to 6th order using residualization techniques. The reduction was accomplished by retaining the states associated with the first and third structural modes and the lowest frequency actuator mode. The second structural mode was not retained because it is primarily a fuselage bending mode. All other states were residualized. Stability analyses were then performed using the reduced-order (6th) controller with the "evaluation model" to assess the stability margins. Several iterations on the input noise and the sensor noise were required before an acceptable design was found. As the input noise was increased, the stability margins would increase but with an associated increase in the controller bandwidth. The bandwidth was decreased by increasing the sensor noise. After a reasonable tradeoff was obtained between increased stability margins and controller bandwidth, the following symmetric and antisymmetric filters were synthesized.

$$G_s=K_s \times\frac{(s+21.33)(s^2+65.94s+18578.00)(s^2+76.78s\ 87202.00)}{(s^2+97.67s+3381.00)(s^2+26.00s+20938.00)(s^2+375.40s+3.58\times 10^5)} \qquad (7a)$$

$$G_a=K_a \times\frac{(s+22.10)(s^2+51.00s+18769.00)(s^2+76.78+87206.00)}{(s^2+68.41s+4419.60)(s^2+18.39s+23076.60)(s^2+278.90s+2.08\times 10^5)} \qquad (7b)$$

To provide good rolloff characteristics at both low and high frequencies, the following filter

$$G_c=\frac{s(1000)^2}{(s+2)(s+1000)^2} \qquad (8)$$

was added to both the symmetric and antisymmetric filters. The final control laws are products of Eqs. (7a) and (8) and Eqs. (7b) and (8).

As determined from Nyquist stability analyses, only the positive gain margin of the symmetric case was less than desired (only +4.7 *dB* instead of +6 *dB* was obtained). This violation in the positive gain margin criteria was accepted at this time for testing at subcritical velocities since it was expected that the control law would be updated.

Analysis at Off-Design Flight Conditions and Gain Scheduling Definition

Nyquist analyses were performed at flight near the respective FSS-off flutter boundaries of both the symmetric and antisymmetric cases with the control laws previously defined. The results of this analysis (not shown) indicated that the Nyquist diagrams were approaching too close to the critical point, thus suggesting that both the symmetric and the antisymmetric loop gains were too large. From inspection of the Nyquist diagrams, the values of K_s and K_a were adjusted to allow the system to have better stability margins. The Nyquist plot of the more critical symmetric case with the adjusted gain in shown in Fig. 5. In a similar manner, Nyquist analyses were performed at other flight conditions from $M=0.700$ to 0.925 at increments of $M=0.025$ to establish a gain schedule. These analyses indicated that the gain schedule only needed to be a function of dynamic pressure. The resulting gain schedule is

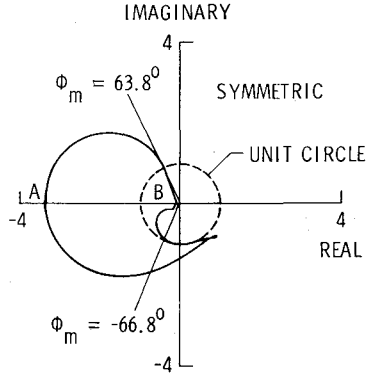

Fig. 5 Nyquist plot near FSS-off flutter boundary, $M=0.85$ at 15,000 ft (symmetric).

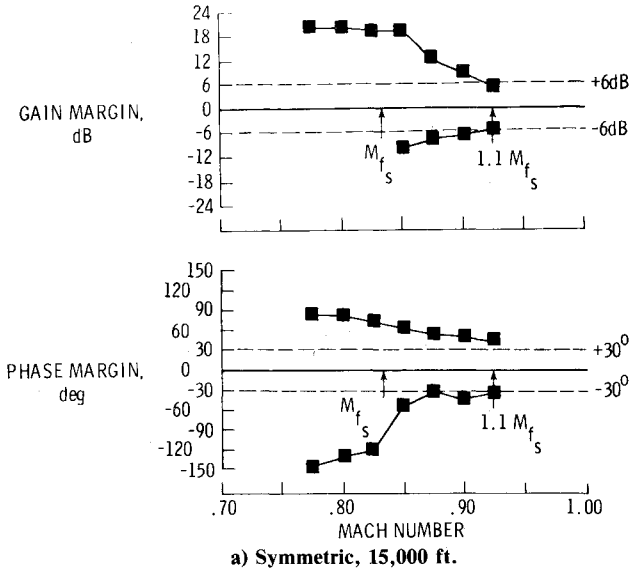

a) Symmetric, 15,000 ft.

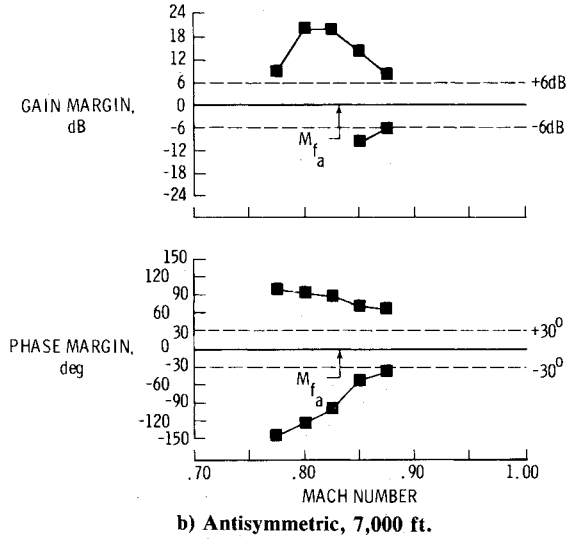

b) Antisymmetric, 7,000 ft.

Fig. 6 Stability margins as a function of Mach number.

given by the following equations:

$$K_s = \begin{cases} 110.70 & 0 < q < 608.40 \text{psf} \\ 110.70 + 3.06(q - 608.40) & 608.40 < q < 720.00 \text{psf} \\ 451.70 & q > 720.00 \text{psf} \end{cases} \tag{9a}$$

$$K_a = \begin{cases} 62.00 & 0 < q < 779.04 \text{psf} \\ 62.00 + 1.63(q - 779.04) & 779.04 < q < 878.40 \text{psf} \\ 223.62 & q > 878.40 \text{psf} \end{cases} \tag{9b}$$

Figure 6 shows the stability magins as a function of Mach number for both the symmetric and antisymmetric cases using the gain schedule given in Eq. 9. The design objectives are met except for the positive gain margin criteria in the symmetric case at $M = 0.925$.

To assess the effect of the control law on the higher-frequency structural modes, a gain root locus calculation was performed. Gain root locus plots are presented in Fig. 7 for

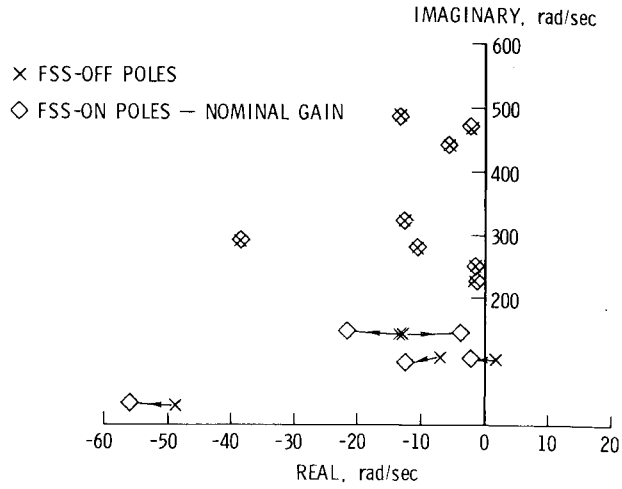

a) Symmetric, 15,000 ft.

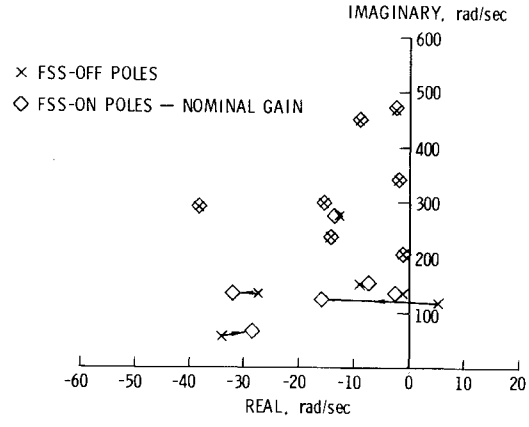

b) Antisymmetric, 7,000 ft.

Fig. 7 Gain root locus with initial control law near FSS-off flutter boundary ($M = 0.85$; arrows indicate increasing gain).

both the symmetric and antisymmetric cases near their respective FSS-off flutter boundaries. The control law affects primarily the modes below 200 rad/s and leaves the higher frequency modes relatively unaffected as indicated by the fact that the poles for the FSS-off are essentially coincident with the poles at nominal gain.

Figure 8 shows the flutter boundaries for both the FSS-off and FSS-on cases. Both the symmetric and antisymmetric FSS-on flutter speeds are above the 10% increase in the minimum (symmetric) FSS-off flutter speed.

Updated Structural Model

As a result of a ground vibration test (GVT) of the full-up vehicle and the addition of a body conforming external fuel tank to the vehicle, the initial EAL structural model was updated. The natural frequencies, the corresponding vibration mode shapes and the structural dampings of the empty-fuel vehicle[17] were measured during the GVT. This information was used to update the EAL finite-element model by modifications to the structural stiffness. Separate eigenvalue analyses were performed on the empty, mid, and fuel-mass configurations of the updated structural model to obtain vibration frequencies and mode shapes.

The FSS-off flutter boundaries for the three fuel configurations are shown in figures 9a and 9b. Note that for the symmetric mid-fuel configuration the flutter boundaries for the initial EAL model and the updated EAL model differ by over 2,000 ft (updated model indicates that the flutter boundary is at a higher Mach number and at a corresponding lower

altitude). In an effort to keep the flight Mach number below $M=0.925$ at the 10% increase in flutter speed (to minimize transonic effects), it was decided to lower the altitude for flight testing from 15,000 to 13,000 ft. All further calculations presented in this paper will be for an altitude of 13,000 ft. The empty fuel configuration results in the minimum symmetric flutter speed, whereas the full fuel configuration results in the minimum antisymmetric flutter speed.

Evaluation of Control Law with Updated Structural Model

Stability analyses were performed using the control law defined by Eq. (7) and (8) and the gain schedule of Eq. (9) with the updated structural model. In addition, a new actuator model was also used in this analysis which will be presented in the next section. The updated structural model and the new actuator model are considered to be the best description of the aircraft dynamics prior to the first flight test of the ARW-1R wing.

Figure 10 shows the stability margins as a function of Mach number at 13,000 ft for both the symmetric and antisymmetric mid-fuel conditions. Analyses were also performed for the other fuel conditions, but only the mid-fuel condition results are presented. For the symmetric case, the gain margins meet the design objectives except for a small violation in the negative gain margin at $M=0.925$. The negative gain margin is very large near the flutter boundary (approximately -18 *dB*) which indicates that the gain is too large. The positive phase margins meet the design objectives up through $M=0.925$. However, the negative phase margins fall short of the design objective between $M=0.85$ and 0.89. From an inspection of the Nyquist diagrams at these Mach numbers (not shown), it was determined that the small negative phase margins are a result of the gain being too large. For the antisymmetric case, all of the stability margins meet the design objectives up through $M=0.915$. However, both the negative gain margins and the negative phase margins fall short of the design objectives between $M=0.915$ and 0.925. From an inspection of the Nyquist plot at $M=0.925$ (not shown), it was determined that the gain was too small for this condition. The need for these gain changes can be attributed to changes in the flutter speed

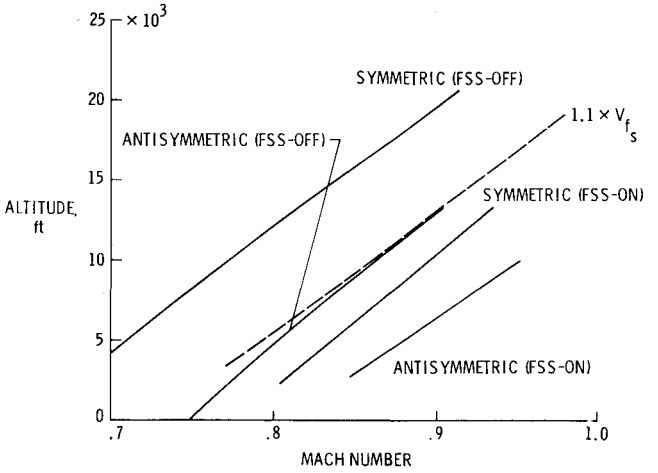

Fig. 8 Flutter boundary with the control law defined by Eq. (7) and gain schedule of Eq. (9).

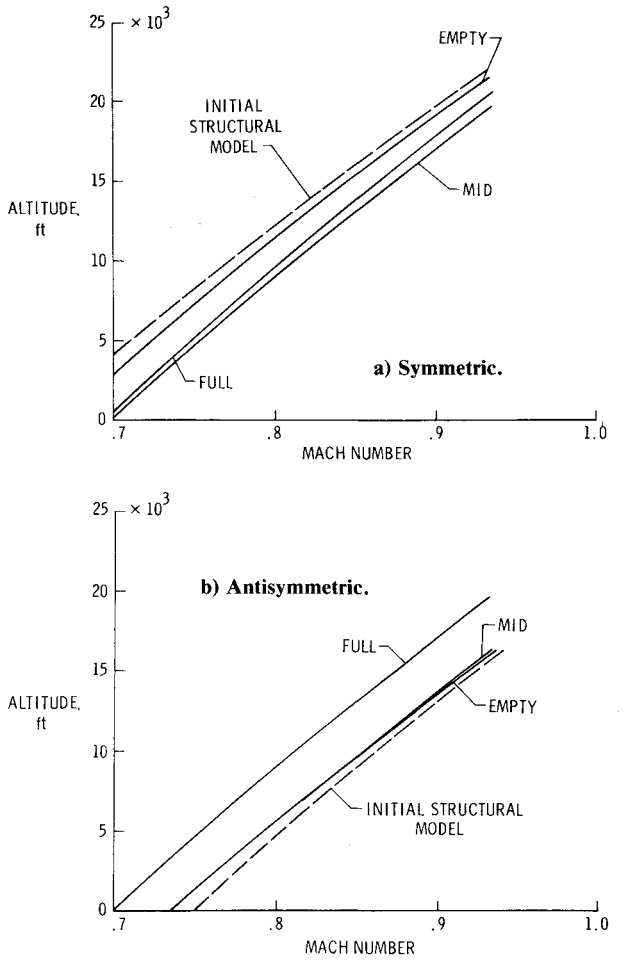

Fig. 9 FSS-off flutter boundary of the updated ARW-1R model at various fuel weight conditions.

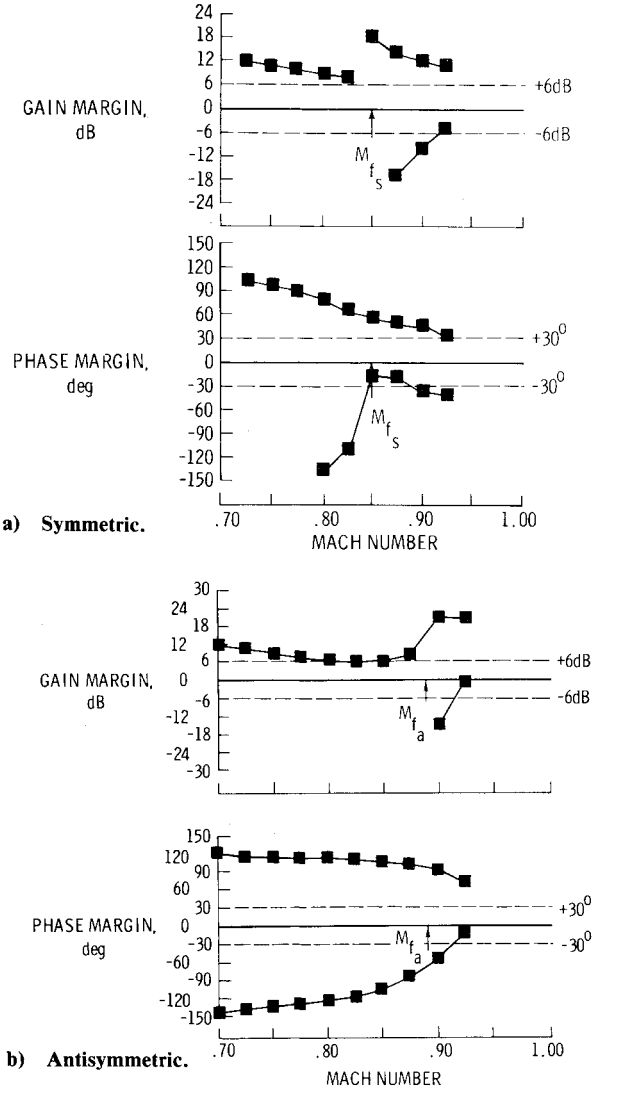

Fig. 10 Stability margins as a function of Mach number at 13,000 ft.

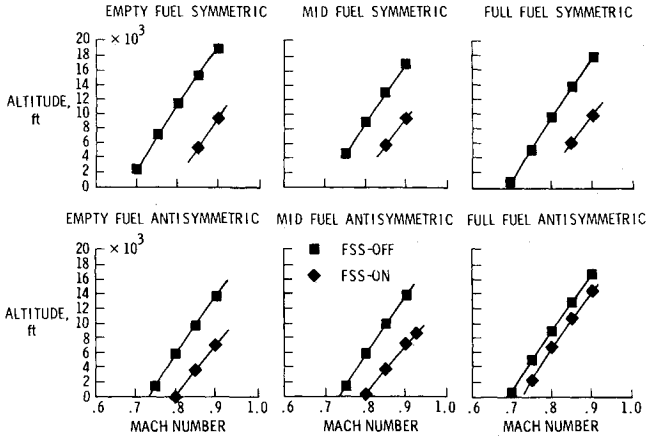

Fig. 11 Flutter boundaries with the updated ARW-1R model at various weight conditions using gain scheduled control law.

as a consequence of differences betwen the initial mathematical model and the updated mathematical model.

Figure 11 shows the flutter boundaries for all three of the fuel conditions. In all cases the flutter speed is increased with the FSS-on. The empty weight symmetric case has the largest increase. The full weight antisymmetric case has the smallest increase in flutter speed.

Experimental Activities

The system configuration is identical to the previous ARW-1 system.[14] The FSS is implemented as an analog system onboard the aircraft. During the ground tests, frequency response measurements of the FSS were made and compared well with predicted results.

It was required that the FSS exhibit a $+6$ *dB* gain margin on the ground. Tests were performed to establish this gain margin. These tests involved turning the FSS on and increasing the gain until either the $+6$ *dB* gain margin was reached or an instability occurred. If instabilities occur, notch filters of the form

$$\frac{s^2+2\zeta_N\omega_N s+\omega_N^2}{s^2+2\zeta_D\omega_D s+\omega_D^2}$$

are used to eliminate them. Notch filters are first implemented in the actuator loop. In this implementation does not eliminate the instability, then notch filters are implemented directly in the FSS loop. The test was performed and required the implementation of several notch filters in the actuator loop before a $+6$ *db* gain margin could be achieved.

The dominant effect of the notch filters is to reduce the bandwidth of the actuator. The frequency response of the actuator with the notch filters was curve fitted to obtain the model used in the evaluation of the control law with the updated structural model. The resulting transfer model of the actuator is given as

$$\frac{\delta}{\delta_c}=\frac{1.99\times 10^{10}}{(s^2+299.40s+9.13\times 10^4)(s^2+344.67s+2.46\times 10^5)} \tag{10}$$

Conclusions

The design of the flutter suppression system for a remotely-piloted research vehicle has been discussed. As shown in this paper optimal control techniques can be used to synthesize flutter suppression control laws in a viable and systematic fashion. The design objective of increasing the minimum flutter speed by 10% while maintaining ± 6 *dB* and ± 30 deg stability margins was achieved except for a $+4.7$ *dB* gain margin at one flight condition. This was accomplished over a wide range of flight conditions with only gain scheduling required as a function of dynamic pressure. After an update to the mathematical model, stability margins were degraded. In addition, the flutter supression system was not as effective for some off-design fuel conditions. The flutter suppression system was ground-tested to eliminate high-frequency instabilities and to check control system frequency responses.

References

[1]Doggett, R. V., and Townsend, J. L., "Flutter Suppression by Active Controls and Its Benefits," *Proceedings of the SCAR Conference,* NASA CP-001, Nov. 9-12, 1976.

[2]Newsom, J. R., "A Method for Obtaining Practical Flutter Suppression Controls Laws Using Results of Optimal Control Theory," NASA TP-1471, Aug. 1979.

[3]Mukhopadhyay, V., Newsom, J. R., and Abel, I., "A Method for Obtaining Reduced-Order Control Laws for High-Order Systems Using Optimization Techniques," NASA TP-1876, 1981.

[4]Mahesh, J. K., Stone, C. R., Garrard, W. L., Dunn, H. J., "Control Law Synthesis for Flutter Suppression Using Linear Quadratic Gaussian Theory," *Journal of Guidance and Control,* Vol. 4, July-Aug. 1981, pp. 415-422.

[5]Gangsaas, D., and Ly, U., "Application of a Modified Linear Quadratic Gaussian Design to Active Control of a Transport Airplane," AIAA Paper 79-1746, Aug. 1979.

[6]Hwang, C., and Pi, W. S., "Application of Optimal Control Techniques to Aircraft Flutter Suppression and Load Alleviation," AIAA 23rd Structures, Structural Dynamics and Materials Conference, New Orleans, La., AIAA Paper 82-0724, May 1982.

[7]Newsom, J. R., Abel, I., and Dunn, H. J., "Application of Two Design Methods for Active Flutter Suppresion and Wind-Tunnel Test Results," NASA TP-1653, May 1980.

[8]Abel, Perry III, B., and Newsom, J. R., "Comparison of Analytical and Wind-Tunnel Results for Flutter and Gust Response of a Transport Wing With Active Controls," NASA TP-2010, 1982.

[9]Johnson, E. H., Hwang, C., Pi, W. S., Kesler, D. F., Joshi, D. S., and Harvey, C. A. "Test Demonstration of Digital Control of Wing/Store Flutter," AIAA 23rd Structures, Structural Dynamics and Materials Conference, New Orleans, La., AIAA Paper 82-0645, May 1982.

[10]Rogers, K. L., Hodges, G. E., and Felt, L., "Active Flutter Suppression—A Flight Demonstration," *Journal of Aircraft,* Vol. 12, June 1975, pp. 551-556.

[11]Peloubet, R. P., Jr., Haller, R. L., and Bolding, R. M., "F-16 Flutter Suppression System Investigation Feasibility Study and Wind Tunnel Tests," *Journal of Aircraft,* Vol. 19, Feb. 1982, pp. 169-175.

[12]Murrow, H. N., and Eckstrom, C. V., "Drones for Structural Testing (DAST)—A Status Report," *Journal of Aircraft,* Vol. 16, Aug. 1979, pp. 521-526.

[13]Edwards, J. W., "Flight Test Results of an Active Flutter Suppression System Installed on a Remotely Piloted Research Vehicle," AIAA Paper 81-0655, April 1981.

[14]Newsom, J. R., and Pototzky, A. S., "Comparison of Analysis and Flight Test Data for a Drone Aircraft with Active Flutter Suppression," AIAA Paper 81-0640, April 1981.

[15]Bennett, R. M., and Abel, I., "Application of a Flight Test and Data Analysis Technique to Flutter of a Drone Aircraft," AIAA Paper 81-0652, April 1981.

[16]Newsom, J. R., Pototzky, A. S., and Abel, I., "Design of the Flutter Suppression System for DAST ARW-1R—A Status Report," NASA TM 84642, March 1983.

[17]Eckstrom, C. V., and Spain, C. V., "Design Considerations and Experiences in the Use of Composite Material for an Aeroelastic Research Wing," AIAA Paper 82-0678, May 1982.

[18]Whetstone, W. D., "EISI-EAL: Engineering Analysis Language," Proceedings of the Second Conference on Computing in Civil Engineering, American Society of Civil Engineering, 1980, pp. 276-285.

[19]Peele, E. L., and Adams, W. M., Jr., "A Digital Program for Calculating the Interaction Between Flexible Structures, Unsteady Aerodynamics, and Active Controls," NASA TM-80040, Jan. 1979.

[20]Doyle, J. C., and Stein, G., "Robustness With Observers," *IEEE Transactions on Automatic Control,* Vol. AC-24, 1979, pp. 607-611.

[21]Kwakernaak, Huibert, and Sivan, Raphael, "Linear Optimal Control Systems," Wiley Interscience, New York, 1972.